030601-7-T

EFFICIENT FINITE ELEMENT SIMULATION OF SLOT SPIRALS, SLOT RADOMES AND MICROWAVE STRUCTURES

J. Gong and J.L. Volakis

National Aeronautics and Space Administration
Langley Research Center
Hampton, VA 23681-0001

January 1995

THE UNIVERSITY OF MICHIGAN

Radiation Laboratory
Department of Electrical Engineering
and Computer Science
Ann Arbor, Michigan 48109-2122
USA

Report #030601-7-T

NASA Langley Grant NAG 1–1478

Grant Title:	Simulation of Conformal Spiral Slot Antennas on Composite Platforms
Report Title:	Efficient Finite Element Simulation of Slot Spirals, Slot Radomes and Microwave Structures using Prismatic Elements
Report Authors:	J. Gong and J.L. Volakis
Primary University Collaborator:	John L. Volakis
Primary NASA–Langley Collaborator:	Fred Beck Telephone: (804) 864-1829
University Address:	Radiation Laboratory Department of Electrical Engineering and Computer Science Ann Arbor, Michigan 48109–2122 Email: volakis@umich.edu Phone: (313)764-0500
Date:	January 1995

Forward

This progress report contains the following two documents.

- **Efficient Finite Element Simulation of Slot Antennas Using Prismatic Elements.**
  This document describes the implementation of prismatic elements for slot antenna and slot radome simulations. Results are given for slot radomes in comparison with measurements and for spiral antennas. In the latter case, a slot loop is used for code validation and a number of spiral antenna patterns are included to demonstrate the improved gain, CP characteristics and bandwidth of this antenna. The development of the prismatic elements and implementation details are given in our earlier grant report 030601-5-T

- **Application and Design Guidelines of the PML Absorber for Finite Element Simulations of Microwave Packages.**

  This document first gives a review of the anisotropic perfectly matched layer(PML) for mesh truncation which was originally described in our earlier report 030601-5-T. The performance of the PML is then examined for a finite simulation of microwave circuit structures. Our goal in future studies is to employ the finite element method with the PML for the simulation of antenna+microwave circuit integrated structures. In this manner, the feeding network and antenna elements are treated as a single system rather than individually as done in the past.

Efficient Finite Element Simulation of Slot Antennas Using Prismatic Elements

Jian Gong and John L. Volakis
radiation laboratory
University of Michigan
Ann Arbor, MI 48109-2122
jxgum@umich.edu volakis@umich.edu

Abstract

A hybrid finite element - boundary integral (FE-BI) simulation technique is discussed to treat narrow slot antennas etched on a planar platform. Specifically, the prismatic elements are used to reduce the redundant sampling rates and ease the mesh generation process. Numerical results for an antenna slot and frequency selective surfaces are presented to demonstrate the validity and capability of the technique.

1 Introduction

It has been reported that a hybrid finite element–boundary integral technique [Jin, et. al. 1991, Silvester and Pelosi (1994)] can be employed for characterizing conformal antennas of arbitrary shape [Gong, et. al. (1994)]. Indeed, planar/non–planar, rectangular/non–rectangular designs, ring slot or spiral slot antennas with probe, coax cable or microstrip line feeds can be simulated with this formulation. This is because of the geometrical adaptability of tetrahedral elements used for the implementation. However, in practice, certain configurations require extremely high sampling rates due to the presence of fine geometrical details. Among them are a variety of slot antennas (spirals, rings, slot spirals, cross slots, log–periodic slots, etc.), where the slot width is much smaller than the other dimensions (cavity diameter or inter–distance of slots). In these cases, the mesh is extremely dense (with over 50, 100 or even higher samples per wavelength), whereas typical discretizations involve only 10–20 elements per wavelength. This

dense sampling rate is especially severe for 3–D tetrahedral meshes, where the geometrical details usually distort the tetrahedrals. The numerical system assembled from this type of mesh often leads to large system conditions due to the degraded mesh quality. Also, mesh generation is tedious and the solution CPU time is unacceptably large.

In this paper, we propose a finite element–boundary integral formulation using edge–based triangular prism elements. It can be shown that this element choice is ideally suited for planar antenna configurations, including spirals, circular and triangular slots. Among the many advantages of the prismatic elements, the most important is the simplicity of mesh generation. Also, much smaller number of unknowns is required for an accurate and efficient modeling of complex geometries. Below, we begin by first outlining the finite element–boundary integral (FE–BI) formulation for slot antenna modeling. A new, physically meaningful, set of edge–based functions for prisms is then presented to generate the discrete system of equations. The final section of the paper gives results for antenna radiation and transmission through frequency selective surfaces. Comparisons with reference and measured data are given and the efficiency of the implementation is discussed.

2 Formulation

Consider the cavity–backed slot antenna shown in Fig. 1 where the cavity is recessed in a ground plane. To solve for the E–field inside and on the aperture of the cavity, a standard approach is to extremize the functional

$$\begin{aligned} F(\mathbf{E}) &= \frac{1}{2}\iiint_V \{(\nabla\times\mathbf{E})\cdot\overline{\overline{\mu}}^{-1}\cdot(\nabla\times\mathbf{E}) - k_0^2\overline{\overline{\epsilon}}\mathbf{E}\cdot\mathbf{E}\}dV \\ &+ \iiint_{V_s}\mathbf{E}\cdot\left(jk_0Z_0\mathbf{J}_i + \nabla\times\overline{\overline{\mu}}^{-1}\cdot\mathbf{M}_i\right)dV \\ &+ jk_0Z_0\iint_{S_0+S_f}\mathbf{E}\cdot(\mathbf{H}\times\hat{n})\,dS \end{aligned} \tag{1}$$

where $\overline{\overline{\epsilon}}$ and $\overline{\overline{\mu}}$ denote the relative tensor constitutive parameters of the cavity medium, Z_0 and k_0 are the free space impedance and propagation constant, respectively, S_0 represents the aperture excluding the metallic portions and S_f denotes the junction opening to the guided feeding structures. Also, V_s is the volume occupied by the source(s) and $\mathbf{H}$ is the corresponding magnetic field on S_0 and S_f whose outer normal is given by $\hat{n}$. The explicit knowledge of $\mathbf{H}$ in (1) is required over the surface S_0 and S_f (referred to as mesh truncation surfaces) for a unique solution of $\mathbf{E}$. Specifically, the

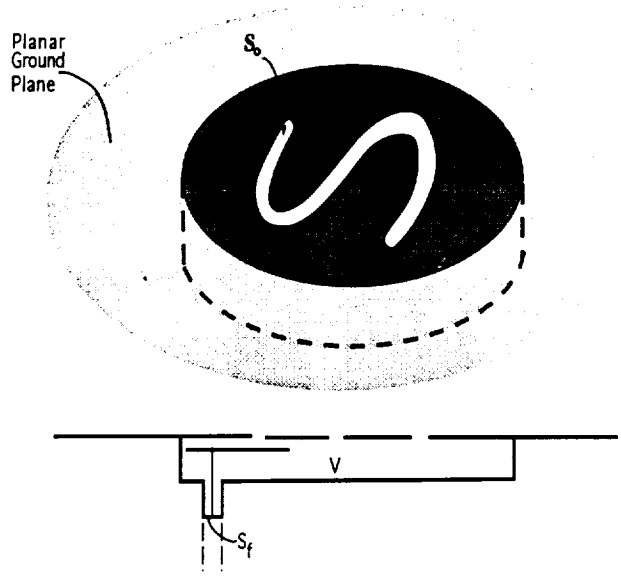

Figure 1: Geometry of cavity–backed microstrip antennas

magnetic field $\mathbf{H}$ over S_0 may be replaced in terms of $\mathbf{E}$ via a boundary integral (BI) or absorbing boundary condition (ABC), whereas $\mathbf{H}$ on S_f is determined on the basis of the given feeding structure. In this paper, we will employ the boundary integral method [Jin, et. al., 1991] for truncating the mesh, a technique commonly referred to as the finite element – boundary integral (FE–BI) method. In the context of the FE–BI, $\mathbf{H}$ is represented by the integral

$$\mathbf{H} = \mathbf{H}^{g0} + \iint_{S_0} [\hat{z} \times \mathbf{E}(\mathbf{r}')] \cdot \bar{\mathbf{G}}(\mathbf{r}, \mathbf{r}')\, ds', \tag{2}$$

where $\bar{\mathbf{G}}$ is the electric dyadic Green's function of the second kind [Tai (1994)] such that $\hat{n} \times (\nabla \times \bar{\mathbf{G}}) = 0$ is satisfied on the (planar, spherical or cylindrical) metallic platform. For the antenna problem shown in Fig. 1 where the platform is a planar ground plane, $\bar{\mathbf{G}}$ becomes the half space dyadic Green's function

$$\bar{\mathbf{G}} = 2jk_0 Y_0 \left(\bar{\mathbf{I}} + \frac{1}{k_0^2}\nabla\nabla\right) \frac{e^{-jk_0|\mathbf{r}-\mathbf{r}'|}}{4\pi|\mathbf{r}-\mathbf{r}'|}, \tag{3}$$

with $\mathbf{r}$ and $\mathbf{r}'$ being the observation and integration points, respectively, and $\bar{\mathbf{I}} = \hat{x}\hat{x} + \hat{y}\hat{y} + \hat{z}\hat{z}$ is the unit dyad. In connection with our problem, i.e.

that of a cavity recessed in a ground plane, $\mathbf{H}^{g0}$ is equal to the sum of the incident and reflected fields for scattering computations, or zero for antenna parameter evaluations.

To discretize the functional (1), we choose to subdivide the volume region using prismatic elements as shown in Fig. 2 and Fig. 3, The field in each of the prisms can be approximated using the linear edge–based expansion [Nedelec (1980), Webb (1993), Bossavit (1989)]

$$\mathbf{E}^e = \sum_{j=1}^{9} E_j^e \mathbf{V}_j^e = [\mathbf{V}]_e^T \{E^e\}, \tag{4}$$

where $[\mathbf{V}]_e = [\{V_x\}, \{V_y\}, \{V_z\}]$, and $\{E^e\} = \{E_1^e, E_2^e, \ldots, E_9^e\}^T$. The vectors $\{V_u\}, u = x, y, z$, are of dimension $m = 9$ and they simply represent the x, y, z components of $\mathbf{V}_j^e$ associated with the jth edge of the eth element. Since $\mathbf{V}_j^e$ are chosen to be edge–based functions, the unknown coefficients E_j^e represent the average field along the jth edge of the eth element. A corresponding representation for the aperture fields is

$$\mathbf{E}(\mathbf{r}) = \sum_{i=1}^{3} E_i^s \, \mathbf{S}_i^s(\mathbf{r}) = [S]_s^T \{E^s\}, \tag{5}$$

where $[S]_s = [S_x, S_y]$, and $\mathbf{V}(\mathbf{r})$ reduces to $\mathbf{S}^s(\mathbf{r})$ when the position vector is on the slot.

To generate the discrete system for E_j^e, (4) and (5) are substituted into (1) and subsequently $F(\mathbf{E})$ is differentiated with respect to each unknown E_j^e. With the understanding that the surface field coefficients E_j^s are a subset of E_j^e, we obtain

$$\left\{ \frac{\partial F_V}{\partial E^e} \right\} = \sum_{e=1}^{N_v} [A^e]\{E^e\} + \sum_{e=1}^{N_s} [B^s]\{E^s\} + \sum_{e=1}^{N_v} \{K_e\} + \sum_{s}^{N_s} \{L_s\} = 0 \tag{6}$$

where the sums are over the total number of volume or surface elements. In this, the matrix elements are given by

$$[A]_e = \iiint_{V_e} \left\{ [DV]_e [\mu_r^{-1}] [DV]_e^T - k_0^2 [V]_e [\epsilon_r]^T [V]_e^T \right\} dv \tag{7}$$

$$\{K\}_e = \iiint_{V_e} [V]_e \left[jk_0 Z_0 \begin{Bmatrix} J_{ix} \\ J_{iy} \\ J_{iz} \end{Bmatrix} + \nabla \times [\mu_r^{-1}] \begin{Bmatrix} M_{ix} \\ M_{iy} \\ M_{iz} \end{Bmatrix} \right] dv \tag{8}$$

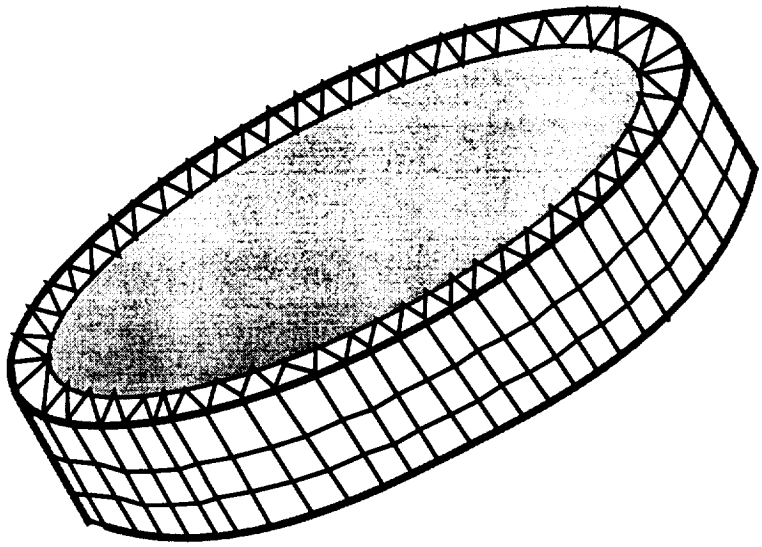

Figure 2: Illustration of tessellation using prisms

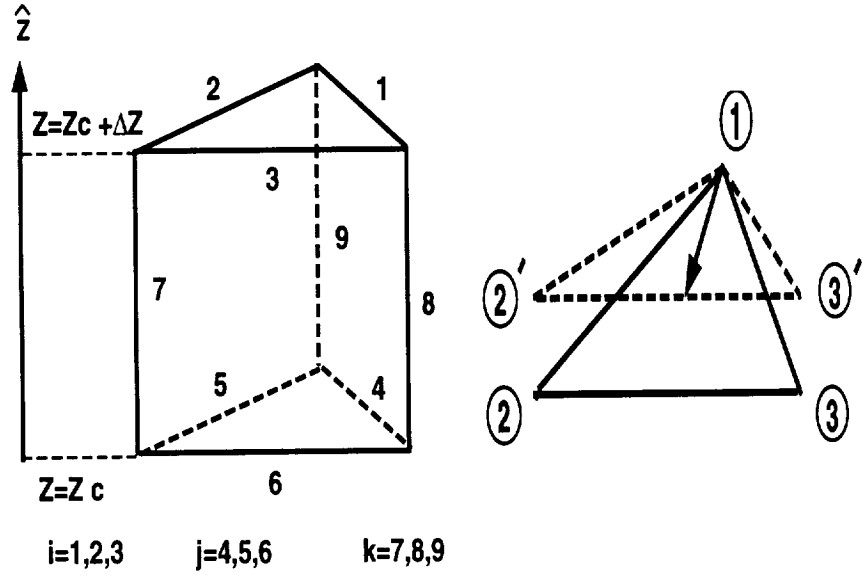

Figure 3: Right angled prism

$$[DV]_e^T = \begin{bmatrix} \frac{\partial}{\partial y}\{V_z\}^T - \frac{\partial}{\partial z}\{V_y\}^T \\ \frac{\partial}{\partial z}\{V_x\}^T - \frac{\partial}{\partial x}\{V_z\}^T \\ \frac{\partial}{\partial x}\{V_y\}^T - \frac{\partial}{\partial y}\{V_x\}^T \end{bmatrix} \tag{9}$$

$$[B^s] = \iint_{S_s}\iint_{S_s'}\{-2k_0^2[S]_s[S]_s^T + 2\left[\frac{\partial}{\partial x}\{S_y\} - \frac{\partial}{\partial y}\{S_x\}\right] \left[\frac{\partial}{\partial x'}\{S_y\}^T - \frac{\partial}{\partial y'}\{S_x\}^T\right]\} \cdot G_0(\mathbf{r},\mathbf{r}')\, dS\, dS' \tag{10}$$

$$\{L_s\} = jk_0Z_0 \iint_{S_s}[S]_s \begin{pmatrix} H_y^{g0} \\ -H_x^{g0} \end{pmatrix} dS \tag{11}$$

where $\{L_s\}$ is removed in case of radiation problems and the same holds for $\{K_e\}$ when the scattering problem is considered.

3 Edge–Based Elements

Consider the right angled prism shown in Fig. 3 whose vertical (z–directed) sides are parallel (right–angled prism). The height of the prism and the triangle area will be designated as

$$h = \hat{e}_i \cdot \hat{z} \times (\mathbf{r} - \mathbf{r}_i), \quad S^e = \frac{l_i}{2}\hat{e}_i \cdot \hat{z} \times (\mathbf{r} - \mathbf{r}_i) \tag{12}$$

where $\mathbf{r}_i$ denotes the location of the ith node, $\hat{e}_i$ is the unit vector along the ith triangular edge, l_i denotes the length of this edge and $\mathbf{r}$ is any position vector terminated inside the triangle. One way to obtain an edge–based field representation for the prism is to utilize the nodal basis functions [Zienkiewicz (1989)] and then apply the procedure discussed in [Nedelec (1980), Bossavit and Mayergoyz (1989)]. However, an alternative and more physically meaningful approach can be employed for the construction of the edge elements. Referring to Fig. 2, it is evident that if $\mathbf{r}$ is in the x–y plane, then S_e in (12) gives the area of another triangle $12'3'$ such that the lengths of edges joining the nodes $2-3$ and $2'-3'$ are equal. With this definition of $\mathbf{r}$, the vector

$$\mathbf{S}_i = \frac{l_i}{2S^e}\hat{z} \times (\mathbf{r} - \mathbf{r}_i) \tag{13}$$

has a magnitude which is equal to the ratio of the areas of the triangle 12'3' to that of 123. We observe that (13) is simply the edge–based expansion for the triangular elements [Rao, et. al. (1982)] and is the appropriate expansion to be used in (5). The corresponding volumetric basis functions can be obtained by inspection, viz.

$$\begin{aligned} \mathbf{V}_i &= \frac{(z-\Delta z)}{\Delta z}\mathbf{S}_i & i &= 1,2,3 \\ \mathbf{V}_j &= \frac{(z_c+\Delta z-z)}{\Delta z}\mathbf{S}_i & j &= 4,5,6 \\ \mathbf{V}_k &= \hat{z}\zeta_k & k &= 7,8,9 \end{aligned} \tag{14}$$

where ζ_k is the triangle simplex coordinate associated with the kth prism vertex at (x_k, y_k). As illustrated in Fig. 3, z_c and $h = \Delta z$ represent the offset coordinate and the prism height, respectively. When (14) are substituted into (7), the resulting integrals can be evaluated in closed form as given in the Appendix. However, the integrals resulting from the substitution of (13) into (10) must be carried out numerically, except the self–cells which must be performed analytically as discussed by Wilton (1981).

4 Applications

Radiation and scattering by an Annular Slot: To evaluate the accuracy and efficiency of the prismatic mesh and the aforementioned implementation, we first consider the analysis of the narrow annular slot (0.75cm wide) shown in Fig. 4. The slot is backed by a metallic circular cavity 24.7 cm in diameter and 3 cm deep. The FE–BI method is quite attractive for this geometry because the slot is very narrow and most of the computational requirements are shifted on the finite element portion of the system. The calculation shown in Fig. 5 were carried out using the prismatic and tetrahedral elements [Gong, et. al. (1994)]. As seen, they overlay each other. However, only 1024 prisms were needed for modeling the cavity, whereas the number of the tetrahedral elements for this homogeneously filled cavity were 2898 for acceptable element distortion. If a multi–layered structure was considered, or a similar system condition was used as a criterion for mesh generation, then much more tetrahedrals than prisms would be needed for modeling such a structure. Moreover, the prismatic mesh is trivially generated given the slot outline. In contrast, substantial time investment is required for generating and post–processing the tetrahedral mesh.

Frequency Selective Surfaces (FSS): FSS structures [Pelton and Munk (1979), Mittra et.al. (1988)] are arrays of tightly packed periodic

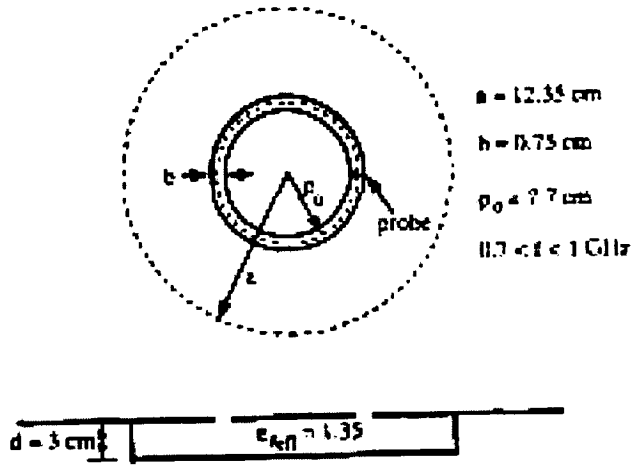

Figure 4: Geometry of the annular slot antenna backed by a cavity 23.7 cm in diameter and 3 cm deep

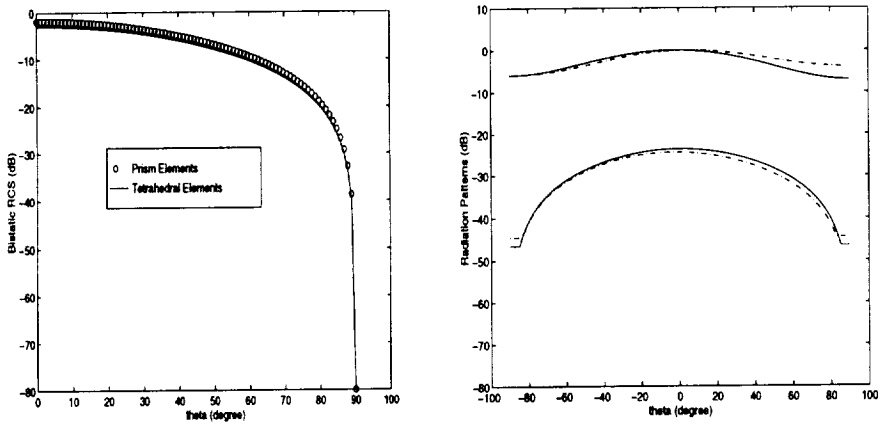

Figure 5: Scattering: Bistatic (co–pol) RCS patterns computed using the tetrahedral FE–BI code and the prismatic FE–BI code. The normally incident plane wave is polarized along the $\phi = 0$ plane and the observation cut is perpendicular to that plane. Radiation: X–pol and Co–pol radiation patterns in the $\phi = 0$ plane from the annular slot antenna shown in figure 4. The solid lines are computed using the tetrahedral FE–BI code whereas the dotted lines are computed using the prismatic FE–BI code. The excitation probe is placed at the point (y=0) marked in figure 4.

elements which are typically sandwiched between dielectric layers. The periodic elements may be of printed form or slot configurations designed to resonate at specific frequencies. As such, they are penetrable around the element resonances and become completely reflecting at other frequencies. To meet bandwidth design specifications, stacked element arrays may be used in conjunction with dielectric layer loading.

Here we shall consider the analysis of FSS structures (with slot elements) via the FE–BI method. Because of the fine geometrical detail associated with the FSS surface, the finite element method has yet to be applied for the characterization of FSS structures, but use of prismatic elements makes this a much easier task. Of particular interest in FSS design is the determination of the transmission coefficient as a function of frequency, and since the array is periodic, it suffices to consider a single cell of the FSS. For computing the transmission coefficient T, the periodic cell is placed in a cavity as shown in Fig. 6 and the structure is excited by a plane wave impinging at normal incidence. Assuming that near resonance the wave transmitted through the FSS screen will retain its TEM character, the transmission line concept can be used to find the scattered field

$$E^s = \frac{\alpha T^2}{1 - \alpha R}$$

where T is the transmission coefficient of the FSS, $R = 1 - T$ and α is the reflection coefficient associated with the cavity base. To reduce the multiple interactions within the cavity, it is appropriate to terminate the cavity with some absorber, thus reducing the value of α to less than 0.1. Then, since R is also small near resonance, a good approximation for T is

$$T_{dB}^{(0)} = 10 \log \left| \frac{E^s}{\alpha} \right|$$

and upon considering the next higher order cavity interactions, we have

$$T_{dB} \approx T_{dB}^{(0)} + 10 \log \left[1 - \alpha (1 - T^{(0)}) \right].$$

A more direct and traditional computation of T_{dB} would involve the placement of the FSS element in a thick slot [Jin and Volakis (1991)]. However, this requires enforcement of the boundary integral over the entire lower surface of the slot, leading to a much more computationally intensive implementation.

The above FSS modeling approach was applied for a characterization of single layer and multi–layer FSS structures. In both cases, the periodic

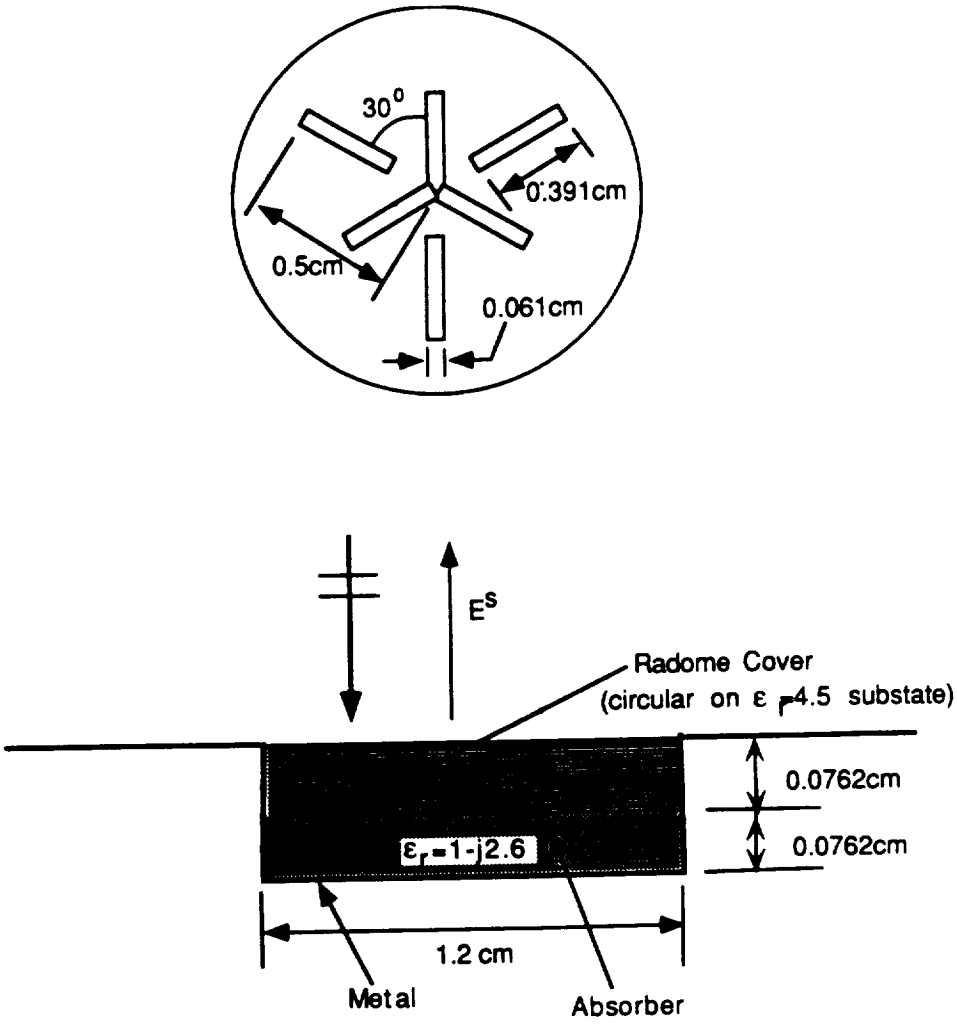

Figure 6: Illustration of the setup for computing the FSS transmission coefficient Upper figure: periodic element (top view); Lower figure: periodic element in cavity (cross-sectional view)

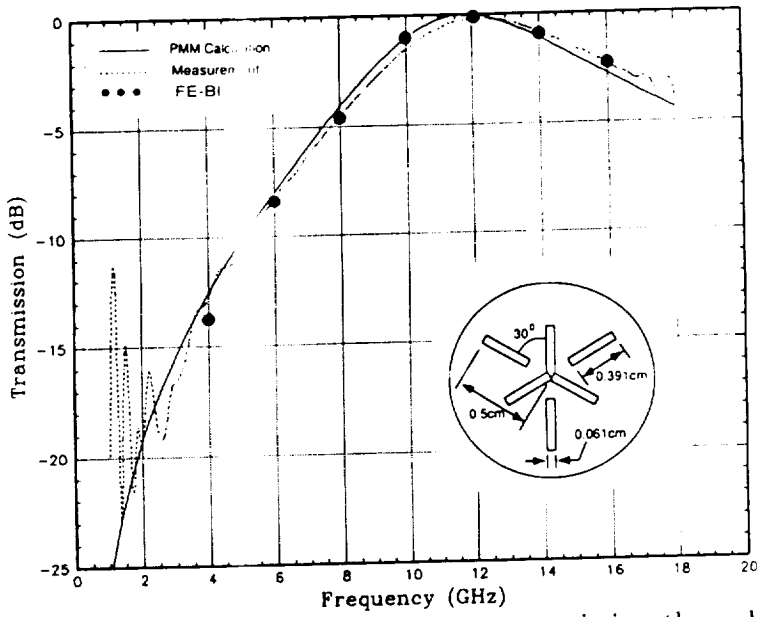

Figure 7: Calculations and comparisons of transmission through the FSS structure shown in Fig. 6

element was a slot configuration. The geometry of the single layer periodic element is shown in Fig. 6 and consists of a planar slot array on a dielectric layer 0.0762 cm thick and having $\epsilon_r = 4.5$. The FE–BI calculation using prismatic elements is given in Fig. 7. Clearly, our calculations are in good agreement with the measurements and data based on the more traditional PMM approach [Berrie (1995), Henderson (1983)].

The geometry of the multilayer radome considered in our study is given in Fig. 8. The total thickness of the FSS was 6.3072cm and is comprised of two slot arrays (of the same geometry) sandwiched within the dielectric layers. For modeling purpose, a 1.54cm thick absorber is placed below the FSS as shown in Fig 8. From the calculated results, it is seen that the results generated by the FE–BI method are in good agreement with the measurements.

Radiation Property study of Conformal Slot Spiral Antenna:

Consider a typical Archemidean slot–spiral antenna shown in Figure 9. This antenna is built on a double–sided PCB with its two arms following the expression: $r = \alpha\theta + \beta$, where $\alpha = 0.1333cm$ and $\beta = 2.8595cm$. One arm can be determined from the other by rotating 180° counterclockwisely. It is noted that this structure differs from the conventional design in that the central portion of the spiral is not fabricated. The reasoning for it relies on

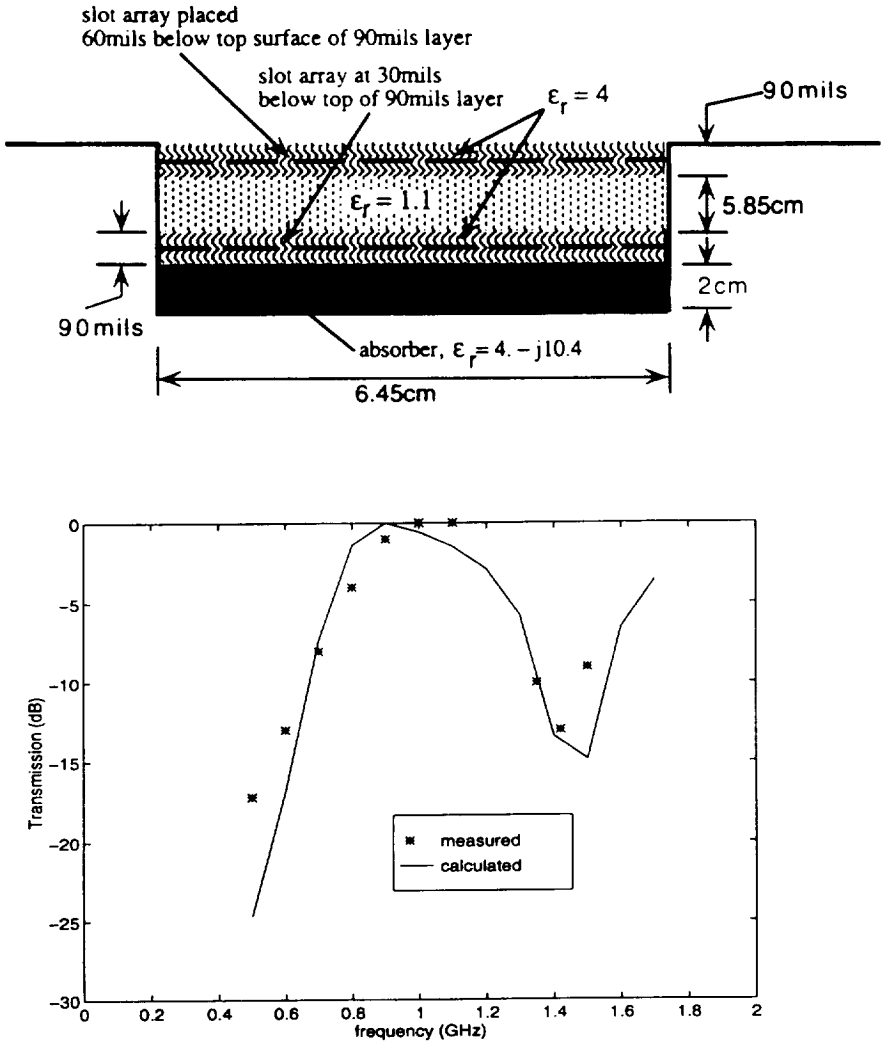

Figure 8: Upper figure: geometry of the multilayer frequency selective surface (FSS) used for modeling; lower figure: measured and calculated transmission coefficient through the FSS structure

the facts that the antenna is designed with a bandwidth less than 30%, and that the central portion usually requires a careful fabrication because of the geometric details, and still that the central space may be used for possibly complex feed network. One of our goal is to study the effect of this spiral shape on its performance.

A benchmark test model is designated to operate from 118 MHz to 157 MHz. to replace the conventional protruding blade antenna. The size however is much compact with its conformality property. Our simulation model is scaled by 1/8 to operate at 944MHz to 1256MHz with the center frequency 1100MHz. The values of α and β above were determined based on this frequency band and also the number of turns (4.5). The cavity is filled with a dielectric slab ($\epsilon_r = 2.2$) of 0.3 cm depth, corresponding to approximately 0.011 free space wavelength at the center frequency. The antenna's directivity is analyzed from the radiated pattern at lower, center and higher frequencies and the results are tabulated in table 1.

Figure 10 – 12 show the radiation patterns for frequency 944, 1100 and 1256 MHz, respectively. The E_θ and E_ϕ at the principle plane $\phi = 90°$ are plotted. It is understood that while the frequency varies, the antenna's active region moves; thus this principle plane may not be the practical 'E–plane' (although the two feeds are placed close to this plane). The optimum axial ratio for the three cases are tabulated also in table 1, and it shows that the spiral shape design really plays an important role to insure a good quality radiation pattern. At both center and lower frequencies, less than 3 dB AR has been achieved. When the frequency increases, the active region moves inwards to the center and becomes closer to the feeds where the EM fields exhibits comparatively strong profile. The radiated pattern therefore is most likely affected and this explains why the AR increases at the high frequency. This can be readily improved by adding a couple of spiral turns inside. It is seen, nevertheless, that a CP mode can be achieved within the entire designated bandwidth and with a wide azimuthal angle (as wide as 60° in the optimum case). In practice, we notice that absorbing materials may be needed to regulate the magnetic currents at the beginning or ends of the slot spiral, especially when the number of turns is minimized. This implementation however is not needed in simulation of this design work.

The further effects of the dielectric property, the depth and the size of the substrate on antenna's radiation performance will be investigated to provide an optimized design for the conformal slot spiral. The miniaturization technique will also be carefully studied and applied to the atenna design with no trade off readiation performance.

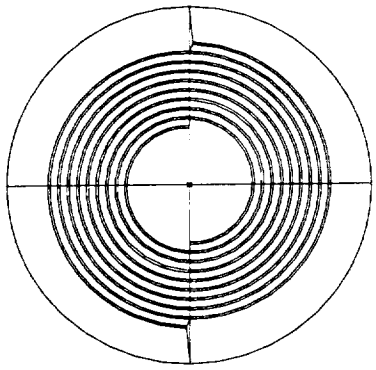

Figure 9: Illustration of a typical 2-arm slot-spiral design

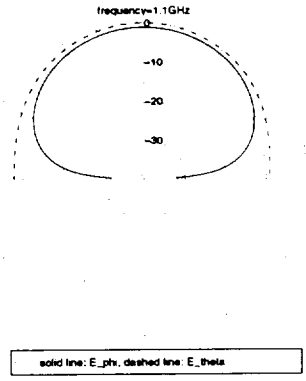

Figure 10: Radiation Pattern at f=1.1GHz (center frequency design). A good axial ratio is achieved up to 60° degree.

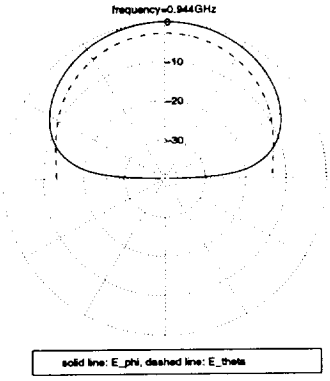

Figure 11: Radiation Pattern at f=0.944GHz (lower end of frequency range). It can be seen that the axial ratio of the pattern becomes larger compared to that at the center frequency, but still remains within 3dB for a wide angle range. This indicates that the number of the outer turns in the spiral contour design is most likely sufficient.

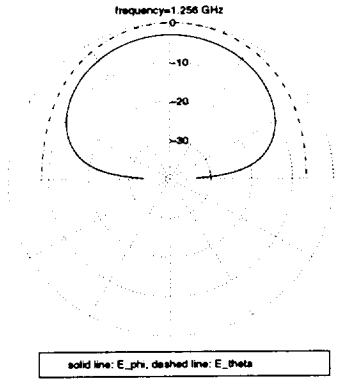

Figure 12: Radiation Pattern at f=1.256GHz (higher end of frequency range). It can be seen that the axial ratio of the pattern is deteriorated compared to those at the center frequency and lower frequency. This certainly shows that the number of inner loops still needs to be increased to insure a good quality pattern.

Frequency (GHz)	0.944	1.100	1.256
Gain (dB)	7.22	6.66	5.23
Axial Ratio (dB)	2.7	1.0	3

Table 1: Comparisons of gain and axial ratio at differnent operating frequencies

5 Conclusion

A hybrid finite element–boundary integral (FE–BI) formulation was presented for modeling narrow slots in metal backed cavities. Prismatic elements were used in connection with the FE–BI implementation, and in contrast to the tetrahedral elements, these offer several advantages. Among them,low sampling rates are needed for generating meshes and the mesh generation process is substantially simplified. Other advantages of the prismatic elements over the tetrahedral elements include better system conditions and faster pre/post data processing.

The explicit expressions for FE–BI implementation of prismatic elements were tabulated and numerical results for slot antennas and frequency selective surfaces were presented to demonstrate the validity and capability of the technique.

Appendix

For FEM implementation, the following quantities are required

$$P^e_{mn} = \int_{V^e} \nabla \times \mathbf{V}_m \cdot \nabla \times \mathbf{V}_n \, dV \tag{15}$$

$$Q^e_{mn} = \int_{V^e} \mathbf{V}_m \cdot \mathbf{V}_n \, dV \tag{16}$$

where the curls are given by

$$\begin{aligned}
\nabla \times \mathbf{V}_i &= -\frac{l_i}{2S^e \Delta z}\left[(x - x_i)\hat{x} + (y - y_i)\hat{y} - \hat{z}(z - z_c)\right] && i = 1,2,3 \\
\nabla \times \mathbf{V}_j &= \frac{l_i}{2S^e \Delta z}\left[(x - x_j)\hat{x} + (y - y_j)\hat{y} + \hat{z}(z_c + \Delta z - z)\right] && j = 4,5,6 \\
\nabla \times \mathbf{V}_k &= \frac{1}{2S^e}\left[(x_{k2} - x_{k1})\hat{x} + (y_{k2} - y_{k1})\hat{y}\right] && k = 7,8,9
\end{aligned} \tag{17}$$

To this end, we follow the notation defined in (13) and (14), where i, i'=1,2,3 represent the top triangle edges, j, j'=4,5,6 denote the bottom triangle edges and k, k'=7,8,9 stand for the vertical three edges. It is found that (16) and (17) can be analytically evaluated and we tabulate the results as follows

$$P_{ii'} = C_{ii'}\left[D_{ii'}\Delta z + \frac{4}{3}S^e(\Delta z)^3\right] \tag{18}$$

$$P_{jj'} = C_{jj'}\left[D_{jj'}\Delta z + \frac{4}{3}S^e(\Delta z)^3\right] \tag{19}$$

$$P_{kk'} = \frac{\Delta z}{4S^e}\bar{l}^k \cdot \bar{l}^{k'} \tag{20}$$

$$P_{ij} = P_{ji} = -C_{ij}\left[D_{ij}\Delta z - \frac{4}{6}S^e(\Delta z)^3\right] \tag{21}$$

$$P_{ik} = P_{ki} = -\frac{l_i}{4(S^e)^2}\left[\hat{x}\cdot\bar{l}^k(SX - x_iS^e) + \hat{y}\cdot\bar{l}^k(SY - y_iS^e)\right] \tag{22}$$

$$P_{jk} = P_{kj} = \frac{l_j}{4(S^e)^2}\left[\hat{x}\cdot\bar{l}^k(SX - x_ijS^e) + \hat{y}\cdot\bar{l}^k(SY - y_jS^e)\right] \tag{23}$$

$$Q_{ii'} = \frac{(\Delta z)^3}{3}C_{ii'}D_{ii'} \tag{24}$$

$$Q_{jj'} = \frac{(\Delta z)^3}{3}C_{jj'}D_{jj'} \tag{25}$$

$$Q_{kk'} = \Delta z S^e T_{kk'} \tag{26}$$

$$Q_{ij} = Q_{ji} = \frac{(\Delta z)^3}{6}C_{ij}D_{ij} \tag{27}$$

$$Q_{ik} = Q_{ki} = Q_{jk} = Q_{kj} = 0 \tag{28}$$

where

$$\begin{aligned} T_{kk'} &= 1/6 \quad for\ k = k';\quad 1/12 \quad for\ k \neq k' \\ C_{ij} &= \frac{l_i l_j}{4(S^e\Delta z)^2} \\ D_{ij} &= SXX - (x_i + x_j)SX + x_ix_jS^e + SYY - (y_i + y_j)SY + y_iy_jS^e \end{aligned} \tag{29}$$

The remaining quantities in the above list of the expressions are defined as

$$\begin{aligned} S^e &= \int_{S^e} dxdy \\ SX &= \int_{S^e} x\,dxdy \\ SY &= \int_{S^e} y\,dxdy \end{aligned}$$

$$
\begin{aligned}
SXX &= \int_{S^e} x^2\,dxdy \\
SYY &= \int_{S^e} y^2\,dxdy \\
SXY &= \int_{S^e} xy\,dxdy
\end{aligned}
$$

These integrals can be expressed in terms of the global coordinates of the three nodes $(X_i, Y_i), (X_j, Y_j), (X_m, Y_m)$. Specifically, assuming that the three nodes i,j and m of a triangle are in counterclockwise rotation, we then have,

$$
S^e = \int_{S^e} dxdy = \frac{1}{2}\begin{vmatrix} 1 & x_i & y_i \\ 1 & x_j & y_j \\ 1 & x_m & y_m \end{vmatrix}
$$

$$
\begin{aligned}
SX &= \int_{S^e} x\,dxdy = \frac{S^e}{3}(X_i + X_j + X_m) \\
SY &= \int_{S^e} y\,dxdy = \frac{S^e}{3}(Y_i + Y_j + Y_m) \\
SXX &= \int_{S^e} x^2\,dxdy = \frac{S^e}{12}\left\{(X_i + X_j + X_m)^2 + \left(X_i^2 + X_j^2 + X_m^2\right)\right\} \\
SYY &= \int_{S^e} y^2\,dxdy = \frac{S^e}{12}\left\{(Y_i + Y_j + Y_m)^2 + \left(Y_i^2 + Y_j^2 + Y_m^2\right)\right\} \\
SXY &= \int_{S^e} xy\,dxdy = \frac{S^e}{12}\{(X_i + X_j + X_m)(Y_i + Y_j + Y_m) \\
&\quad + (X_iY_i + X_jY_j + X_mY_m)\}
\end{aligned}
$$

6 References

Berrie,J. (1995). Personal communication, Mission Research Corp.

Bossavit, A. and Mayergoyz, I. (1989). 'Edge-elements for scattering problems', *IEEE Trans. magnetics*, vol. 25, no. 4, pp. 2816-2821.

Gong, J., Volakis, J.L., Woo, A., and Wang, H. (1994). 'A hybrid finite element boundary integral method for analysis of cavity-backed antennas of arbitrary shape', *IEEE Trans. Antennas Propagat.*, vol. 42, pp. 1233-1242.

Henderson, L.W. (1983), 'The scattering of planar array of arbitrary shaped slot and/or wire elements in stratified dielectric medium', Ph.D. dissertation ElectroScience Lab, Ohio State University

Jin, J.M., Volakis, J.L. and Collins, J.D. (1991). 'A finite element-boundary integral method for scattering and radiation by two- and three-dimensional structures', *IEEE Antennas Propagat. Magazine*, vol. 33, no. 3, pp. 22-32.

Jin, J.M., Volakis,J.L. (1991). 'Electromagnetic scattering by and transmission through a three dimensional slot in a thick conducting plane', *IEEE Trans. Antennas Propagat.*, vol. 39, pp. 534–550.

Mittra, R., Chen, C.H. and Cwik, T. (1988). 'Techniques for analyzing frequency selective surfaces –A review', *Proc. IEEE*, vol. 76, pp. 1593–1615.

Nedelec, J.C. (1980). 'Mixed elements in R^3', *Numer. Math.*, vol. 35, pp. 315-341.

Pelton, E.L. and Munk, B.A. (1979). 'Scattering from periodic arrays of crossed dipoles', *IEEE Trans. Antennas Propagat.*, vol. AP-27, pp. 323–330.

Rao, S.M., Wilton, D.R. and Glisson, A.W. (1982), 'Electromagnetic Scattering by surfaces of arbitrary shape', *IEEE Trans. Antennas Propagat.*, Vol. AP-30, pp. 409–418.

Silvester, P.P. and Pelosi, G. (1994), 'Finite Elements for Wave Electromagnetics — Methods and Techniques', *IEEE Press*

Tai, C.T. (1994), 'Dyadic Green Functions in Electromagnetic Theory', (2nd Ed.) IEEE Press

Webb, J.P. (1993). 'Edge elements and what they can do for you', *IEEE Trans. Magnetics*, pp. 1460-1465.

Wilton, D.R. and Butler, C.M. (1981), 'Effective method for solving integral and integro-differential equations', *Electromagnetics*, vol. 1, pp. 289–308.

Zienkiewicz, O.E. and Taylor, R. (1989). *The Finite Element Method*, 4th ed., New York: McGraw-Hill.

Application and Design Guidelines of the PML Absorber for Finite Element Simulations of Microwave Packages

J. Gong*, S. Legault*, Y. Botros* and J.L. Volakis*

Abstract

The recently introduced perfectly matched layer(PML) uniaxial absorber for frequency domain finite element simulations has several advantages. In this paper we present the application of PML for microwave circuit simulations along with design guidelines to obtain a desired level of absorption. Different feeding techniques are also investigated for improved accuracy.

I. Introduction

In the numerical simulation of 3D microwave circuits using partial differential approaches, it is necessary to terminate the domain with some type of non-reflective boundary conditions. When using frequency domain PDE formulations, such as the finite element method, the standard approach is to employ some type of absorbing boundary conditions(ABCs) [1], [2], [3]. Also, the use of infinite elements [4] or port conditions [5] have been investigated. All of these mesh truncation methods require *a priori* knowledge of the dominant mode fields and, to a great extent, their success depends on the purity of the assumed mode expansion at the mesh truncation surface. Larger computational domains must therefore be used and the accuracy of the technique in computing the scattering parameters could be compromised.

Recently, a new anisotropic (uniaxial) absorber [6] was introduced for truncating finite element meshes. This absorber is reflectionless(i.e. perfectly matched at its interface) for all incident waves, regardless of their incidence angle and propagation constants. As a result, it can be placed very close to the circuit discontinuity and is particularly attractive for terminating the computational domain of high density microwave circuits where complex field distributions could be present.

Although the proposed uniaxial PML absorber has a perfectly matched interface, in practice a finite metal-backed (say) layer must be used which is no longer reflectionless due

*Radiation Laboratory, Department of Electrical Engineering and Computer Science, University of Michigan, Ann Arbor, MI 48109-2122

to the presence of the pec (see Fig. 1). It is therefore of interest to optimize the absorptivity of the layer by proper selection of the parameters to achieve a given reflectivity with a minimum layer thickness. In this paper, we present guidelines for implementing the PML absorber to truncate finite element meshes in microwave circuit simulations. Example microwave circuit calculations are also given to demonstrate the accuracy of the PML absorber, the FEM simulator and the feed model. More examples will be presented at the conference.

II. Absorber Design

An extensive study was carried out using two-dimensional(see Fig. 1) and three dimensional models (see Fig. 2) in order to optimize the absorber's performance using the minimum thickness and discretization rate. As expected, the absorber's thickness, material properties and the discretization rate all play an equally important role on the performance of the PML. The typical field behavior interior to the absorber is shown in Fig. 3. As seen, for small β values the field decay is not sufficient to eliminate reflections from the metal backing. For large β values, the rapid decay can no longer be accurately modeled by the FEM simulation and consequently the associated VSWR increases to unacceptable values. However, an optimum value of β which minimizes the reflection coefficient for a given layer thickness and discretization can found. The parameters β and t play complimentary roles and the study shows that the PML absorber's performance can be characterized in terms of the product $\frac{\beta t}{\lambda_g}$ (a scalable quantity when $\alpha = 0$) and the discretization rate. A two-dimensional analysis was carried out to determine the optimum values of $\frac{\beta t}{\lambda_g}$ and N (the number of samples in the PML layer) for maximum absorption near normal incidence. It was determined that given a desired reflection coefficient $|R|$ for the PML absorber, the optimum $\frac{\beta t}{\lambda_g}$ and N values are approximately given by the expressions [7]

$$\frac{\beta t}{\lambda_g} = -0.0106|R| + 0.0433$$

$$N = 0.147 \exp\left[7.353 \frac{\beta t}{\lambda_g}\right]$$

where $|R|$ must be given in dB and N is equal to or exceeding the right hand value. As an example, if we desire to have a value of $|R|$ equal to $-50dB$, from the above formulae we have that $\frac{\beta t}{\lambda_g} \approx 0.58$ and $N = 10$. It should be noted that though the design formulae were derived with $\alpha = 0$ they also hold for small non-zero values of α.

III. Feed Excitation

Two feed models were used in conjunction with the scattering parameter extraction method. One was the horizontal current probes (Fig. 2) linking the back PEC wall with the beginning of a microstrip feed line. About 3 to 5 horizontal probes were needed for convergence and this scheme proved more accurate that the usual single vertical probe.

The other feeding scheme employed here involved the specification of the quasi-static TEM mode at the microstrip line port. In the context of the FEM, the excitation is introduced by imposing boundary conditions across the entire cavity cross section through the

input port. These conditions also serve to suppress backward reflections from the modeled circuit discontinuity. Consequently, they can be placed close to the discontinuity without compromising the accuracy of the scattering parameter extraction.

IV. 3D Modeling Examples

The PML performance as predicted by the formulae was investigated by using it to truncate the domain of 3–D microwave circuits. For example, Fig. 4 shows the optimum value of $\frac{\beta t}{\lambda_g} \approx 0.96$ obtained from the above design equations compares well with the results of the full wave FEM analysis of the microstrip line shown in Fig. 2. The 3–D FEM computations were carried out using $N = 5$ for modeling the PML absorber across its thickness and from the given formulae, it follows that $R = -41dB$ and this agrees well with the optimum value shown in Fig. 4. Another example is the meander line shown in Fig. 5. For the FEM simulation, the structure was placed in a rectangular cavity of size $5.8mm \times 18.0mm \times 3.175mm$. The cavity was tessellated using $29 \times 150 \times 5$ edges and only 150 edges were used along the y-axis. The domain was terminated with a 10 layer PML, each layer being of thickness $t = 0.12mm$. The S_{11} results are shown in Fig 6 and are in good agreement with the measured data [8].

References

[1] R.L. Higdon, "Absorbing boundary conditions for acoustic and elastic waves in stratified media," *J. Comp. Phys.*, Vol. 101, pp. 386-418, 1992.

[2] T.B.A. Senior and J.L. Volakis, *Approximate Boundary Conditions in Electromagnetics*, IEE Press, London, 1995.

[3] J-S. Wang and R. Mittra, "Finite Element Analysis of MMIC structures and electronic packages using absorbing boundary conditions," *IEEE Trans. Microwave Th. and Techn.*, Vol. 42, pp. 441-449, March 1994.

[4] S. Tsitsos, A. Gibson and A. McCormick,"Higher Order Modes in Coupled Striplines: Prediction and Measurement," *IEEE Trans. Microwave Th. and Techn.*, Vol. 42, pp. 2071-2077, Nov. 1994.

[5] J.F. Lee, "Analysis of Passive Microwave Devices by Using three-dimensional tangential vector finite elements," *Int. J. Num. Model.: Electronic Net., Dev. and Fields*, Vol. 3, pp. 235-246, 1990.

[6] Z.S. Sacks, D.M. Kingsland, R. Lee and J.F. Lee, "A perfectly matched anisotropic absorber for use as an absorbing boundary condition," to appear in *IEEE Trans. Antennas Propagat.*

[7] S. Legault, T.B.A. Senior and J.L. Volakis, "Design of Planar Absorbing Layers for Domain Truncation in FEM Applications," submitted to *Electromagnetics.*

[8] I. Wolf, "Finite Difference Time–domain Simulation of Electromagnetic Fields and Microwave Circuits," *International Journal of Microwave and Millimeter–Wave Computer–Aided Engineering*, August 1992.

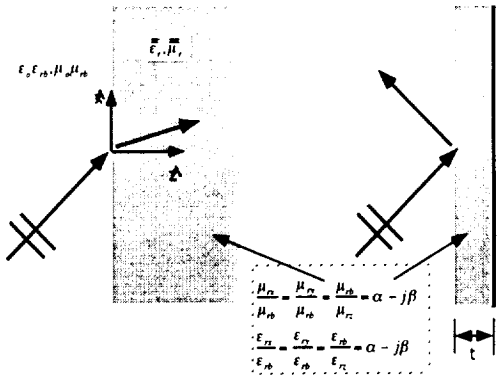

Figure 1: Illustration of wave incidence upon a perfectly match interface (PML) with and without metal backing.

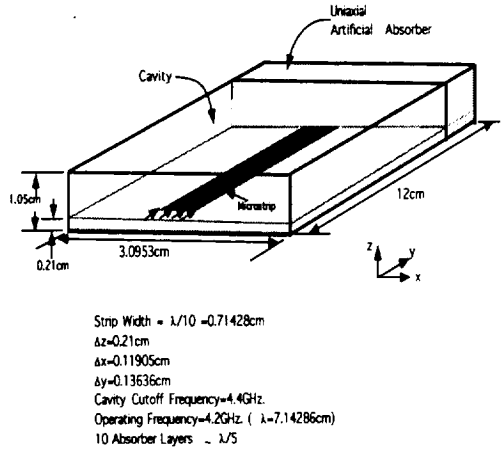

Figure 2: Shielded microstrip line terminated by a perfectly matched uniaxial absorber layer.

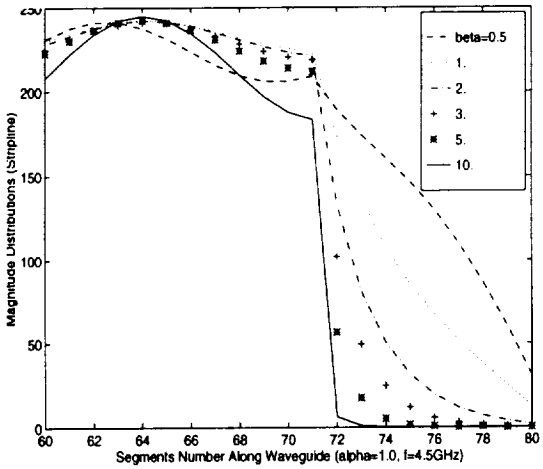

Figure 3: Illustration of the field decay pattern inside the PML layer.

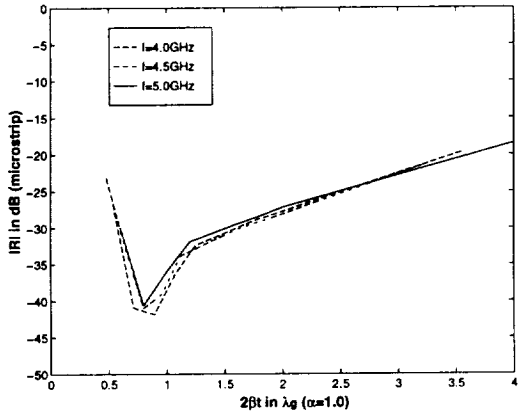

Figure 4: Reflection coefficient vs $2\beta t/\lambda_g$ with α=1, for the shielded microstrip line terminated by the perfectly matched uniaxial layer.

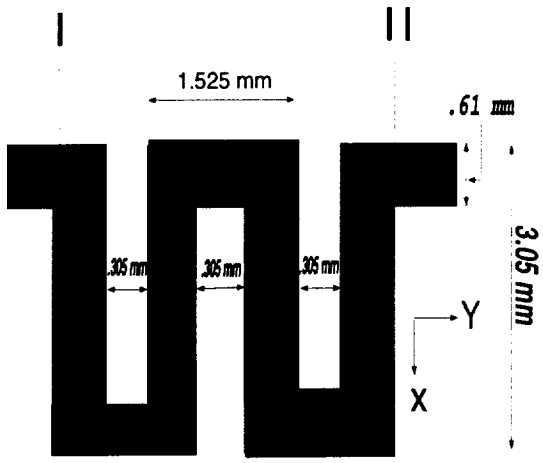

Figure 5: Illustration of a meander line geometry used for comparison with measurement.

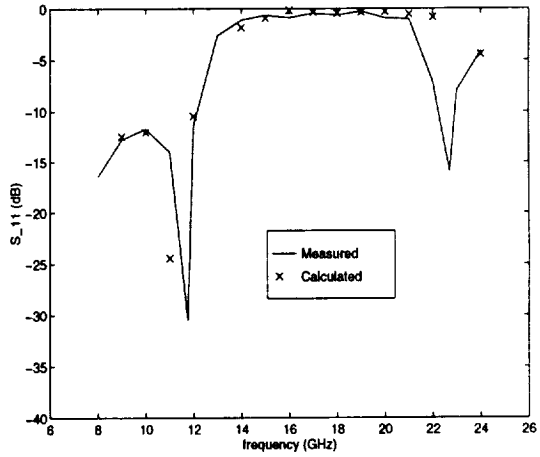

Figure 6: Comparison of calculated and measured results for the meander line shown in Fig.5.